

William Herschel Telescope site characterization using the MOAO pathfinder CANARY on-sky data

O.A. Martin^a, C. M. Correia^a, E. Gendron^b, G. Rousset^b, F. Vidal^b, T.J. Morris^c, A.G. Basden^c, R.M. Myers^c, Y.H. Ono^a, B. Neichel^a, and T. Fusco^{a,d}

^aAix Marseille Université, CNRS, LAM, Laboratoire d'Astrophysique de Marseille, Marseille, France, 38 rue F. Joliot-Curie, 13388 Marseille Cedex 13, France

^bLESIA, Observatoire de Paris – Paris Sciences et Lettres – CNRS – Université Paris Diderot – Sorbonne Paris Cité – Université P. et M. Curie – Sorbonne Université, 5 Place Jules Janssen, 92190 Meudon, France

^cCentre for Advanced Instrumentation, Durham Univ., South Road, Durham, DH1 3LE, UK

^dONERA (Office National d'Etudes et de Recherches Aérospatiales), B.P.72, F-92322 Châtillon, France

ABSTRACT

CANARY is the Multi-Object Adaptive Optics (MOAO) pathfinder for the future MOAO-assisted Integral-Field Units (IFU) proposed for Extremely Large Telescopes (ELT). The MOAO concept relies on tomographically reconstructing the turbulence using multiple measurements along different lines of sight.

Tomography requires the knowledge of the statistical turbulence parameters, commonly recovered from the system telemetry using a dedicated profiling technique. For demonstration purposes with the MOAO pathfinder CANARY, this identification is performed thanks to the Learn & Apply (L&A) algorithm, that consists in model-fitting the covariance matrix of WFS measurements dependant on relevant parameters: $C_n^2(h)$ profile, outer scale profile and system mis-registration.

We explore an upgrade of this algorithm, the Learn 3 Steps (L3S) approach, that allows one to dissociate the identification of the altitude layers from the ground in order to mitigate the lack of convergence of the required empirical covariance matrices therefore reducing the required length of data time-series for reaching a given accuracy. For nominal observation conditions, the L3S can reach the same level of tomographic error in using five times less data frames than the L&A approach.

The L3S technique has been applied over a large amount of CANARY data to characterize the turbulence above the William Herschel Telescope (WHT). These data have been acquired the 13th, 15th, 16th, 17th and 18th September 2013 and we find $0.67''/8.9\text{m}/3.07\text{m.s}^{-1}$ of total seeing/outer scale/wind-speed, with $0.552''/9.2\text{m}/2.89\text{m.s}^{-1}$ below 1.5 km and $0.263''/10.3\text{m}/5.22\text{m.s}^{-1}$ between 1.5 and 20 km. We have also determined the high altitude layers above 20 km, missed by the tomographic reconstruction on CANARY, have a median seeing of $0.187''$ and have occurred 16% of observation time.

Keywords: Multi-object adaptive optics, CANARY, WHT, tomography, turbulence profiling, system mis-registrations, PSF reconstruction

1. INTRODUCTION

For Wide-Field Adaptive Optics (WFAO) systems, the turbulence is compensated in a large Field Of View (FoV) using a tomographic reconstruction of the phase in the entire volume (^{1,2}) or in discrete directions (³), from Wave-Front Sensor (WFS) measurements distributed over the system FoV.

Knowledge of the statistical turbulence parameters is paramount, with several methods being dedicated to estimating them as SLODAR (^{4,5}), MASS (⁶) and SCIDAR (⁷) techniques.

Further author information: olivier.martin@lam.fr

As a MOAO on-sky demonstrator, CANARY has been observing at the William Herschel Telescope (WHT) since 2010 (8). Since an open-loop configuration is adopted, the lack of feedback between the Deformable Mirror (DM) and WFS makes the control more sensitive to inaccuracies on the command matrix calibration. The recursive nature of a closed-loop tends to wash out these effects, which clearly is not the case here.

Vidal et al has proposed in³ the the Learn & Apply (L&A) technique that combines both turbulence profiling and system mis-registration identification/calibration. The efficiency of this method has been demonstrated on-sky with CANARY (8–10,17). The L&A consists in model-fitting the spatial covariance matrix of WFS measurements. The fitting is ensured thanks to the Levenberg-Marquardt iterative algorithm which estimates a number of model-parameters, as the $C_n^2(h)$ profile, the outer scale profile and the stars position. In view of calibration, the primary model proposed by Vidal³ included system mis-registration: pupil shifts, rotation and magnification between WFS.

We used in the past a model³ based on a Fourier transformation of the Von-Kármán spectrum to get the bi-dimensional (2D) spatial covariance of the wave-front slopes. The algorithm was particularly efficient when coupled to wave-front sensors with fixed sub-aperture sizes, because the computation using fast Fourier transforms (FFT) could be used to extract in one shot from the same 2D map all the covariance values between two wave-front sensors with arbitrary separation, without requiring any re-interpolation of the map -provided the sub-aperture size is a multiple of the FFT sampling.

Now, the cone effect inherent to LGS induces layer-projected sub-aperture sizes and pupil sizes to vary with the altitude, which breaks the efficiency of the implementation when it's a matter of computing covariances between LGS and NGS. At least, an interpolation procedure could be implemented in order to access values that lay between covariance samples of the FFT, but unfortunately this kind of approximation does not go well with a fitting procedure that internally requires to compute derivatives as finite differences of the covariance function. We propose thus in Sect. 2 a fast-computable model that includes both turbulence characteristics and system mis-registration.

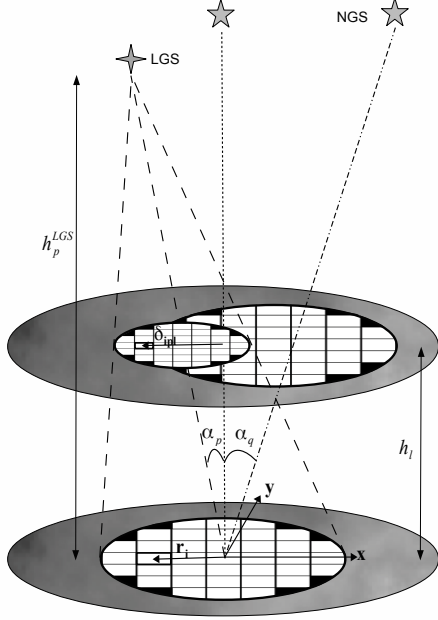
To speed up the fitting algorithm, we propose in Sect.3 an upgrade to the L&A, called the *Learn 3 steps (L3S)*, that splits the identification of the ground layer parameters from those of altitude layers. The ground layer is known to dominate the turbulence strength with relatively slow time-variations (11). It appears thus that a large time-span of accumulated data would be required to obtain statistical convergence on the generation of the covariance matrices of phase (?), the latter being an input to the tomography. In splitting the ground and altitude parts, we mitigate the mis-convergence of statistics obtained from system telemetry.

In addition, we have included in the L3S a separate estimation of the wind-speed profile. From the turbulence profile, we reconstruct the phase at each retrieved altitude using an MMSE approach. The wind-speeds on those layers is then determined from the Full Width at Half Maximum (FWHM) of the average temporal auto-correlation function of slopes.

We present then in Sect. 4 a characterization of the turbulence along altitude above the WHT from the CANARY on-sky data acquired in September 2013. We have processed about 2,000 data sets with the L3S algorithm to present plots of distribution of the seeing, outer scale and wind-speed. We have also characterized the median values for the ground layer (below 1.5 km) the altitude layers (between 1.5 and 20 km) and the very high altitude layers (above 20 km) inaccessible to tomography with CANARY. We conclude in Sect. 5.

2. MODELING THE SPATIAL COVARIANCE OF WFS SLOPES ON TOP OF MIS-REGISTRATION

2.1 Analytic expressions of the covariance



Variable	Description
\mathbf{r}_i	Coordinates of the sub-aperture i in the pupil plane
α_p	Angular position of p^{th} stars from the center of the FoV
h_l	altitude of the l^{th} turbulent layer
δ_{ipl}	Coordinates of the i^{th} sub-aperture of the p^{th} WFS at the altitude h_l
x_{ipl}	Component of δ_{ipl} over the x-axis
y_{ipl}	Component of δ_{ipl} over the y-axis
h_p^{LGS}	Focus altitude of the p^{th} WFS.
d_i	Size of the i^{th} sub-aperture in the pupil plane
$\Delta x_p, \Delta y_p$	Pupil shifts for the p^{th} WFS
θ_p	Rotation shift for the p^{th} WFS
M_p	Magnification for the p^{th} WFS

Figure 1: **Left:** Illustration of the geometry of the tomographic problem. For LGS WFSs, the pupil footprint decreases with altitude because of the cone effect. The coordinates of each LGS slope are affected by a homothety factor. **Right:** Notations used along this paper.

In this proceeding, we review the calculations from^{7, 12} in a more general way, in including system mis-registration. Consider the i^{th} sub-aperture of the p^{th} WFS. In the pupil plane, we note \mathbf{r}_i the position of the i^{th} sub-aperture which does not depend on the actual WFS since all are conjugated at the pupil plane. We include DM/WFS mis-registrations: for the p^{th} WFS, we define Δx_p and Δy_p as the x and y pupil shifts, θ_p as the rotation and M_p as the magnification. We note \mathbf{r}'_i as the new i^{th} sub-aperture's coordinates in the pupil:

$$\mathbf{r}'_i = \begin{bmatrix} \cos(\theta_p) & -\sin(\theta_p) \\ \sin(\theta_p) & \cos(\theta_p) \end{bmatrix} \times [M_p \times \mathbf{r}_i] + \Delta x_p + \Delta y_p \quad (1)$$

We note α_p as the angular position of the p^{th} WFS from the center of the FoV. We will finally note h_p^{LGS} the altitude focus of guide stars and δ_{ipl} as the coordinate of this sub-aperture, at the l^{th} layer, in the pupil plane. We have :

$$\delta_{ipl} = \begin{cases} \alpha_p h_l + \mathbf{r}'_i \left(1 - \frac{h_l}{h_p^{\text{LGS}}} \right) & \text{for a LGS WFS and } h_l \leq h_p^{\text{LGS}}. \\ \alpha_p h_l + \mathbf{r}'_i & \text{for a NGS WFS} \end{cases} \quad (2)$$

For the following theoretical developments, we define x_{ipl} and y_{ipl} the projection of δ_{ipl} on the reference pupil plane:

$$\delta_{ipl} = x_{ipl}\mathbf{x} + y_{ipl}\mathbf{y}, \quad (3)$$

where \mathbf{x} and \mathbf{y} are forming an orthonormal basis along directions x and y . For a Shack-Hartmann WFS, the 2D slopes' map is obtained from the average phase gradient over the lenslet :

$$\mathbf{S}(\delta_{ipl}) = \frac{1}{d_i} \iint_{\mathcal{A}} \nabla \phi(u_i, v_i) du_i dv_i, \quad (4)$$

where d_i is the i^{th} sub-aperture size, i.e. the edge to edge distance in the pupil plane considering all sub-apertures are squared, and \mathcal{A} is the square integration domain comprised between $-d_i/2$ and $d_i/2$ in x and y directions. The integration variables u_i v_i are related to the i^{th} sub-aperture and are given by $u_i = x - x_{ipl}$ and $v_i = y - y_{ipl}$. The x-axis and y-axis slopes are the scalar product between $\mathbf{S}(\boldsymbol{\delta}_{ipl})$ and respectively \mathbf{x} and \mathbf{y} . In projecting the slopes along x or y directions, the integral on sub-aperture surface in Eq. 4 becomes integrals along sub-aperture side :

$$\begin{aligned}\mathbf{S}(\boldsymbol{\delta}_{ipl}) \cdot \mathbf{x} &= \frac{1}{d_i} \int_{-d_i/2}^{d_i/2} dv_i (\phi(x_{ipl} + d_i/2, v_i) - \phi(x_{ipl} - d_i/2, v_i)) \\ \mathbf{S}(\boldsymbol{\delta}_{ipl}) \cdot \mathbf{y} &= \frac{1}{d_i} \int_{-d_i/2}^{d_i/2} du_i (\phi(u_i, y_{ipl} + d_i/2) - \phi(u_i, y_{ipl} - d_i/2)).\end{aligned}\tag{5}$$

We then define the spatial covariance G_{xx} , G_{yy} and G_{xy} as following:

$$\begin{aligned}G_{xx}(\boldsymbol{\Delta}_{ijpq}) &= \langle (\mathbf{S}(\boldsymbol{\delta}_{ipl}) \cdot \mathbf{x})(\mathbf{S}(\boldsymbol{\delta}_{jql}) \cdot \mathbf{x})^t \rangle \\ G_{yy}(\boldsymbol{\Delta}_{ijpq}) &= \langle (\mathbf{S}(\boldsymbol{\delta}_{ipl}) \cdot \mathbf{y})(\mathbf{S}(\boldsymbol{\delta}_{jql}) \cdot \mathbf{y})^t \rangle \\ G_{xy}(\boldsymbol{\Delta}_{ijpq}) &= \langle (\mathbf{S}(\boldsymbol{\delta}_{ipl}) \cdot \mathbf{x})(\mathbf{S}(\boldsymbol{\delta}_{jql}) \cdot \mathbf{y})^t \rangle,\end{aligned}\tag{6}$$

where $\boldsymbol{\Delta}_{ijpq} = \boldsymbol{\delta}_{ipl} - \boldsymbol{\delta}_{jql}$ is the separation between the i^{th} sub-aperture of p^{th} WFS and the g^{th} sub-aperture of q^{th} WFS, at altitude h_l . We develop here the method to get $G_{xx}(\boldsymbol{\Delta}_{ijpq})$ only; both $G_{yy}(\boldsymbol{\Delta}_{ijpq})$ and $G_{xy}(\boldsymbol{\Delta}_{ijpq})$ are similarly derived. Noting the averaged gradient is the difference of phase along each side of the sub-aperture, we then get :

$$\begin{aligned}G_{xx}(\boldsymbol{\Delta}_{ijpq}) &= \frac{1}{d_i d_j} \iint dv_i dv_j \langle (\phi(x_{ipl} + d_i/2, v_i + y_{ipl}) - \phi(x_{ipl} - d_i/2, v_i + y_{ipl})) \\ &\quad (\phi(x_{jql} + d_j/2, v_j + y_{jql}) - \phi(x_{jql} - d_j/2, v_j + y_{jql})) \rangle.\end{aligned}\tag{7}$$

We now use the identity:

$$2(A - a)(B - b) = -(A - B)^2 + (A - b)^2 + (a - B)^2 - (a - b)^2,\tag{8}$$

which allows to rewrite Eq. 7 as follows:

$$\begin{aligned}G_{xx}(\boldsymbol{\Delta}_{ijpq}) &= \frac{1}{2d_i d_j} \iint dv_i dv_j \langle -(\phi(x_{ipl} + d_i/2, v_i + y_{ipl}) - \phi(x_{jql} + d_j/2, v_j + y_{jql}))^2 \\ &\quad - (\phi(x_{ipl} - d_i/2, v_i + y_{ipl}) - \phi(x_{jql} - d_j/2, v_j + y_{jql}))^2 \\ &\quad + (\phi(x_{ipl} + d_i/2, v_i + y_{ipl}) - \phi(x_{jql} - d_j/2, v_j + y_{jql}))^2 \\ &\quad + (\phi(x_{ipl} - d_i/2, v_i + y_{jql}) - \phi(x_{jql} + d_j/2, v_j + y_{jql}))^2 \rangle\end{aligned}\tag{9}$$

Considering $D_\phi(\boldsymbol{\rho}) = \langle (\phi(\mathbf{r}) - \phi(\mathbf{r} + \boldsymbol{\rho}))^2 \rangle$ as the phase Structure Function (SF), we have the final expression of the x-axis slopes covariance :

$$\begin{aligned}G_{xx}(\boldsymbol{\Delta}_{ijpq}) &= \frac{1}{2d_i d_j} \iint dv_i dv_j \left(-2D_\phi \left(\boldsymbol{\Delta}_{ijpq} + \frac{d_i - d_j}{2} \mathbf{x} + (v_i - v_j) \mathbf{y} \right) \right. \\ &\quad \left. + D_\phi \left(\boldsymbol{\Delta}_{ijpq} + \frac{d_i + d_j}{2} \mathbf{x} + (v_i - v_j) \mathbf{y} \right) + D_\phi \left(\boldsymbol{\Delta}_{ijpq} - \frac{d_i + d_j}{2} \mathbf{x} + (v_i - v_j) \mathbf{y} \right) \right) + t_{xx},\end{aligned}\tag{10}$$

where t_{xx} is a constant value to include the telescope tracking error and vibrations we assume to provide an additional isoplanatic tip-tilt to the turbulence. We now consider $W_\phi(\mathbf{k})$ as the Von-Kármán spatial Power Spectral Density (PSD) given by :

$$W_\phi(\mathbf{k}) = 0.023r_0^{-5/3} \left(|\mathbf{k}|^2 + 1/L_0^2 \right)^{-11/3},\tag{11}$$

The phase Structure Function (SF) is related to the spatial PSD $W_\phi(\mathbf{k})$ by :

$$D_\phi(\boldsymbol{\rho}) = 2 \iint_{\mathbb{R}^2} W_\phi(\mathbf{k}) (1 - e^{2i\pi\mathbf{k}\boldsymbol{\rho}}) d\mathbf{k}. \quad (12)$$

where the phase SF following the von-Kármán statistics is :

$$D_\phi(\boldsymbol{\rho}) = \frac{2^{1/6}\Gamma(11/6)}{\pi^{8/3}} \left[\frac{24}{5}\Gamma(6/5) \right]^{5/6} \left(\frac{L_0(h_l)}{r_0(h_l)} \right)^{5/3} \left[\frac{\Gamma(5/6)}{2^{1/6}} - \boldsymbol{\rho}^{5/6} K_{5/6}(\boldsymbol{\rho}) \right], \quad (13)$$

with $\rho = 2\pi |\boldsymbol{\Delta}_{ijpq}| / L_0(h_l)$. In the same way, we get:

$$\begin{aligned} G_{yy}(\boldsymbol{\Delta}_{ijpq}) &= \frac{1}{2d_i d_j} \iint du_i du_j \left(-2D_\phi \left(\boldsymbol{\Delta}_{ijpq} + \frac{d_i - d_j}{2} \mathbf{y} + (u_i - u_j) \mathbf{x} \right) \right. \\ &\quad \left. + D_\phi \left(\boldsymbol{\Delta}_{ijpq} + \frac{d_i + d_j}{2} \mathbf{y} + (u_i - u_j) \mathbf{x} \right) + D_\phi \left(\boldsymbol{\Delta}_{ijpq} - \frac{d_i + d_j}{2} \mathbf{y} + (u_i - u_j) \mathbf{x} \right) \right) + t_{yy}, \end{aligned} \quad (14)$$

and

$$\begin{aligned} G_{xy}(\boldsymbol{\Delta}_{ijpq}) &= \frac{1}{2d_i d_j} \iint du_j dv_i \left(-D_\phi \left(\boldsymbol{\Delta}_{ijpq} - \left(u_j - \frac{d_j}{2} \right) \mathbf{x} + \left(v_i - \frac{d_i}{2} \right) \mathbf{y} \right) \right. \\ &\quad - D_\phi \left(\boldsymbol{\Delta}_{ijpq} - \left(u_j + \frac{d_j}{2} \right) \mathbf{x} + \left(v_i + \frac{d_i}{2} \right) \mathbf{y} \right) \\ &\quad + D_\phi \left(\boldsymbol{\Delta}_{ijpq} - \left(u_j - \frac{d_j}{2} \right) \mathbf{x} + \left(v_i + \frac{d_i}{2} \right) \mathbf{y} \right) \\ &\quad \left. + D_\phi \left(\boldsymbol{\Delta}_{ijpq} - \left(u_j + \frac{d_j}{2} \right) \mathbf{x} + \left(v_i - \frac{d_i}{2} \right) \mathbf{y} \right) \right) + t_{xy}. \end{aligned} \quad (15)$$

To retrieve the solution, the integrals need be discretized along sub-apertures sides. In ^(?,12), this issue is solved using a mid-point version of the Hudgin model : the phase gradient is calculated in taking only the mid-point edge-to-edge phase difference. In such a case, instead of having the integrand variables u_i and v_i ranging from $-d_i/2$ to $d_i/2$, they are evaluated at a single point, equating the integral to zero. In so doing we find again the analytic expression in ^(?,12). This approach allows to drastically reduce the computation time of analytic covariance matrices, few seconds with 8 7x7 SH WFS on CANARY. The cost is an overestimation of 15% on the covariance peak ^(?), but the wings of the spatial covariance are still well reproduced. Overall the covariance model depends on the following parameters :

- n_l : number of discrete layers.
- h_l : altitude layers.
- $r_0(h_l)$: r_0 value for the discrete altitude at altitude h_l
- $L_0(h_l)$: L_0 value for the discrete altitude at altitude h_l
- $\Delta x_p, \Delta y_p, \theta_p$ and M_p : system mis-registration.
- t_{xx}, t_{yy} and t_{xy} : constant value on the covariance map for taking into account telescope tracking error and vibrations.

2.2 Covariance of the aliasing

The covariance of the aliased phase can be derived using Eqs. 10, 14 and 15. These equations involve an expression of the phase SF which depends on the turbulence parameters and the system geometry – Eq. 13. To get the aliasing contribution in the covariance, we have to split the phase into a parallel part, i.e. compensated by the system, and an orthogonal part:

$$\phi = \phi^{\parallel} + \phi^{\perp}. \quad (16)$$

The orthogonal phase contains only spatial frequencies higher than $1/2d$, the DM cut-off frequency. In the case of a Fried geometry (most frequent configuration using SH WFS), the WFS sub-aperture spacing is equal to the DM actuators pitch. Considering then $L_0 \gg 2d$, the aliasing SF $D_\phi^\perp(\boldsymbol{\rho})$ becomes

$$D_\phi^\perp(\boldsymbol{\rho}) = 0.046r_0^{-5/3} \iint_{1/2d}^{\infty} \mathbf{k}^{-11/3} (1 - e^{-2i\pi\mathbf{k}\boldsymbol{\rho}}) d\mathbf{k}. \quad (17)$$

Using Eq. 17 to replace the SF expression in Eqs. 10, 15 and 15, we get an analytic expression of the spatial covariance of the aliasing.

3. LEARN 3-STEPS APPROACH

3.1 L3S concept

For determining the model parameters listed in Sect. 2.1, we use an extension of the Learn&Apply algorithm. This extension is called the *Learn 3 steps* and operates similarly to the latter.

The main idea of the Learn technique is to least-squares fit the empirical covariance matrix from telemetry to the theoretical one. To mitigate the presence of noise we exclude the diagonal of these matrices during the minimization, for which we employ an iterative Levenberg-Marquardt Algorithm (LMA). This method has been demonstrated to be powerful for performing the tomography on CANARY (8).

With the L3S we try to reduce the sensitivity of the model-fitting procedure to the lack of convergence we have on the empirical covariance using short time-series of data. We aim to reach the same tomographic error on a shorter time series than we would with the retrieved parameters of the original method. From the following observation (?): the convergence effect is stronger when the turbulence gets a larger seeing and a slower wind, we take it that the ground layer is the one which contributes the most to this effect. We propose to retrieve it independently from the altitude layers. We report in Fig. 2 a diagram of the L3S algorithm:

- **Step 1:** we start by removing the tip-tilt mode in measurement and model for each WFS. Then we remove the mean slopes between all the WFS corresponding to the ground layer (GL) contribution in both measurement and model. In doing that we suppress the GL contribution of the covariance matrices in order to focus on the altitude layer identification. By applying the LMA on such matrices, we get an estimation of $r_0(h_l)$ and $L_0(h_l)$ in altitude.
- **Step 2:** We get back to the initial values of covariance matrices, always tip-tilt removed, in keeping the same parameters in altitude retrieved during the previous step. The LMA gives then an estimation of the ground layer seeing and outer scale.
- **Step 3:** Finally, we add back the tip-tilt components in the measurements and model covariance matrices. We then retrieve the telescope tracking error and vibrations coefficients t_{xx}, t_{yy} and t_{xy} . They simulate an isoplanatic tip-tilt added to the turbulent one. During this third step, we have also the possibility to retrieve the system mis-registration $\Delta x_p, \Delta y_p, M_p$ and θ_p .

3.2 Performance comparison

We compare the L3S approach with the initial L&A approach proposed by Vidal (3). For only considering the gain on spitting the identification of relevant parameters in three steps, we use exactly the same covariance matrix model in the both cases. We call thus *Learn 1 step* (L1S) the version of the L3S where we retrieve all the parameters during a single step.

We have selected three data sets acquired by CANARY in 2013, comprising 10,000 frames sampled at 150 Hz. Data sets are the concatenation of slopes measured by three off-axis NGS WFS in a 2' field, one one-axis WFS and four Rayleigh LGS WFS. These later were focused at 21 km and positioned at 23" off-axis in a square configuration (10)

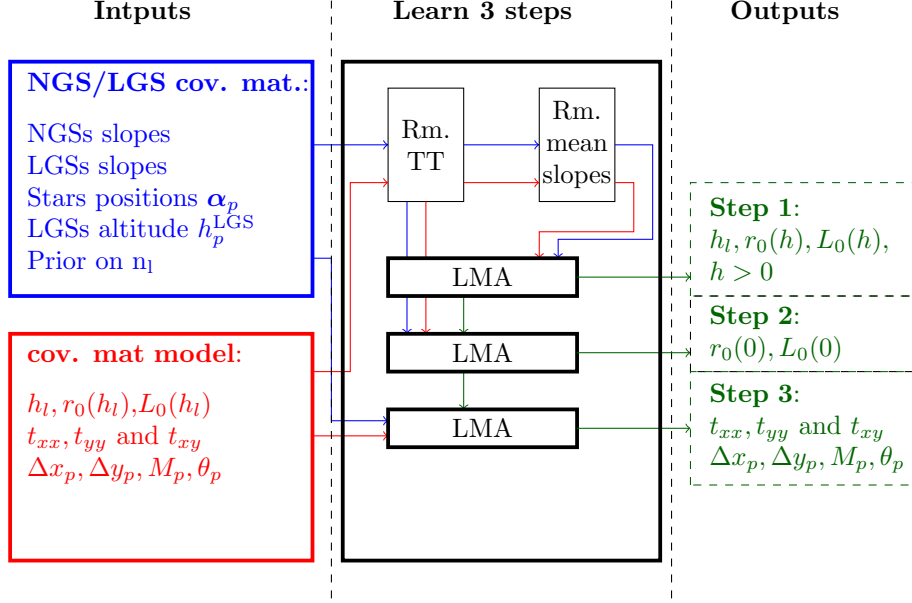


Figure 2: Schematic of the Learn 3 steps algorithm. In blue, red and dark green, we have the paths of respectively the covariance matrix from measurements, from model and the model parameters. On the left, the inputs are the telemetry and the phase gradient covariance matrix model. On the center, the algorithms operates several iterative LMA model-fitting of the measurements' covariance matrix. See text for further details.

We report in Tab. 1 the observation conditions we got for these three cases. To be more accurate on the estimation of the turbulence parameters during the observation, all of these values have been evaluated on the entire 10,000 frames.

Case	1	2	3
Date	09/16/2013	09/17/2013	09/18/2013
Hour	23h58m	00h13m	23h16m
Seeing (")	1.40	0.89	0.310
Altitude seeing	0.20	0.27	0.12
Ground seeing	1.37	0.82	0.26

Table 1: Table of observation conditions for the three studied cases. The ground layer gathers all the layer below 1 km, that corresponds to the tomographic resolution we have with CANARY ⁽⁹⁾.

We have split each of these data sets into two parts: the 5,000 first frames form the *calibration set* while the 5,000 last form the *test set*. We select n_f frames in the calibration set to compute the empirical covariance matrix. In using either the L&A or L3S method, we retrieve two different sets of model parameters. Then, from the model-fitted covariance matrices, we derive a MMSE reconstructor \mathbf{R} and then a Wave Front (WF) *tomographic error* in nm rms ⁽¹²⁾, in applying this reconstructor on the test set. We redo these operations for different values of n_f in order to get the evolution of the tomographic error as function of n_f .

In Fig. 3, we show the tomographic error versus n_f for both L1S and L3S, for the three different sets. In addition in Fig. 3, we compare turbulent profiles retrieved with $n_f = 5,000$ frames for both methods. We get an improvement of the tomographic error on the three cases following two criteria:

- **Better robustness to the lack of convergence of empirical covariance** : tomographic errors with the L3S method are decreasing faster than the L1S ones. It means we reach the same level of accuracy on

the turbulence parameters identification in using around five times less frames in nominal conditions.

- **Better accuracy** : As it appears in Fig. 3, tomographic error plateaus when the time-series length is large enough. The final value of tomographic error we get with the L3S is smaller than the one given by the L1S method. For a time-series of 5,000 frames, we get an improvement on the quadratic error of 50%, 30% and 12% for sets 1, 2 and 3 respectively. This gain is thus increasing with the seeing. Indeed, for worse observation conditions than nominal ones, the mis-convergence of turbulence statistic parameters impacts more the L1S parameter retrieval.

The same is confirmed by the turbulent profiles retrieved by the two approaches : for data set 1, the seeing is worse than nominal conditions (median of 0.7") but the L&A has retrieved weak altitude layers. In comparing with the L3S results, they are fake layers coming from a lack of convergence of the LMA which did not reach the optimal solution. It would be necessary to get many more frames to make the L1S algorithm converging towards this solution, which is in that case a very strong ground layer only. The L3S allows to identify this ground layer only from few thousands frames only.

3.3 Wind-speed profiling

The temporal properties of the turbulence are required for data analysis, LQG control (13) and PSF reconstruction (see paper 9909-64 *PSF reconstruction validated using on-sky CANARY data in MOAO mode* in that conference). In that last case, considering we are seek to reconstructing a long-exposure PSF, the knowledge of wind direction is no longer required. The long-exposure PSF results from an average over all directions. We thus only need to estimate the wind-speed profile.

We discuss here another approach than ones developed from external profiler as SCIDAR (14) or SLODAR (15) based on a cross spatio-temporal covariance fitting. It is based on the temporal auto-covariance function of slopes acquired on NGS WFS in loop disengaged. Such a technique has been also used on RAVEN, the Subaru telescope technical and science MOAO demonstrator (16). We start by reconstructing the WFS slopes layer-by-layer, using the knowledge of the vertical distribution of the turbulence we learn previously from the L3S approach. Then, we determine the FWHM of the temporal auto-correlation function of slopes, which is related to the wind speed according a calibrated relation.

3.3.1 Wind-speed measurements from FWHM temporal auto-correlation function

We note $\mathbf{S}(i, p)$ as the i^{th} measurements provided by the p^{th} WFS. It is a n_f -size vector where n_f is the time-series length. The temporal auto-covariance function of $\mathbf{S}(i, p)$ is $\gamma(i, p)$ and comes from a two-dimensional Fourier transform:

$$\gamma(i, p, \Delta t) = \mathcal{F}^{-1} \left(|\mathcal{F}(\mathbf{S}(i, p))|^2 \right) (\Delta t) \quad (18)$$

We then average the $\gamma(i, p, \Delta t)$ functions over x and y -axis measurements and NGS WFS to get the n_f -sized vector $\bar{\gamma}$:

$$\bar{\gamma}(\Delta t) = \frac{1}{n_s n_{ngs}} \times \sum_{p=1}^{n_{ngs}} \sum_{i=1}^{n_s} (\gamma(i, p, \Delta t) - \sigma_\eta^2(i, p)), \quad (19)$$

where $\gamma(i, p, \Delta t)$ is denoised by the noise variance $\sigma_\eta^2(i, p)$ estimated by interpolating the auto-covariance peak. Finally, we evaluate τ as the FWHM of $\bar{\gamma}(\Delta t)$. The wind-speed depends on the ratio d/τ where d is the sub-aperture size in the pupil plane, actually 0.6 m for CANARY in phase B. Our purpose is now to calibrate the relation between the real wind-speed on-sky assuming a Taylor-like turbulence and the ratio d/τ .

Using the end-to-end simulation tool YAO (<https://github.com/frigaut/yao.git>), we have generated phase screens with nominal seeing ($r_0 = 20$ cm) and outer scale ($L_0 = 9$ m) with different wind-speed values and wind direction comprised between 0 and 2π . We use our routine to determine the ratio d/τ and compare this value to the set wind-speed in YAO to get the factor to be applied to d/τ .

In order to get as close as possible to the on-sky conditions, we have created phase screens of size 50 m times 2048 frames(our acquisition time on-sky). We have performed this comparison for wind-speed spanning from 0 to 10 m.s^{-1} , which corresponds to the range of values we have to deal with on-sky using CANARY . At each velocity value, YAO has generated eight different phase screens from which we acquire system telemetry without

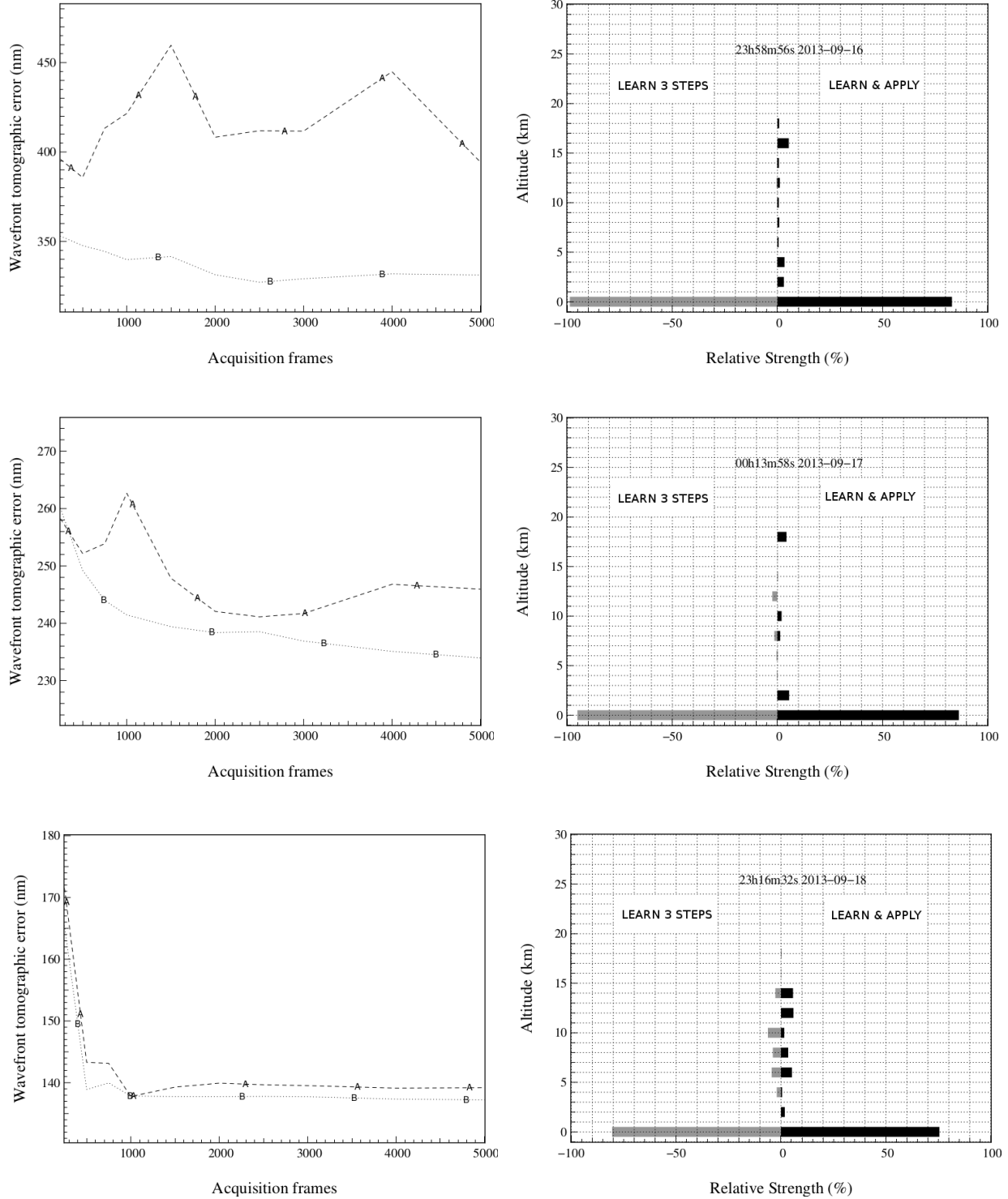
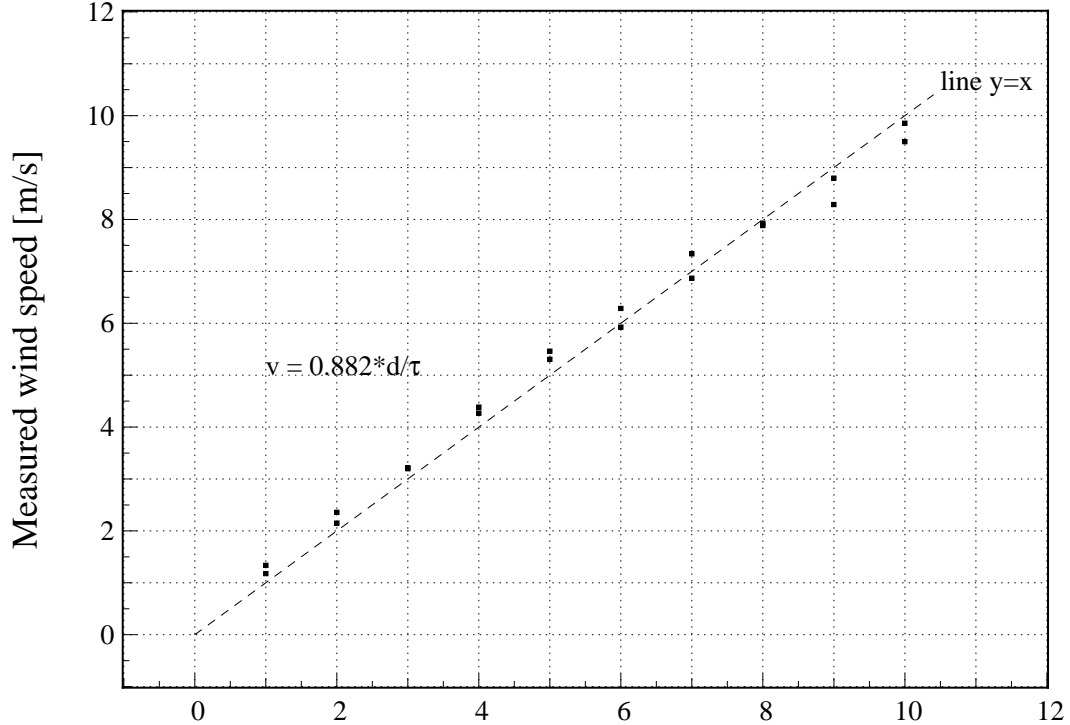


Figure 3: **Left** : Tomographic error got using both the L&A and L&A 3-steps algorithms for retrieving the turbulence properties, for three different cases where the seeing was respectively equal to 1.4, 0.9 and 0.3 arcsec. A: Learn-1-step approach B: Learn 3-steps. **Right** : Comparison between profiles retrieved using either L&A algorithm or Learn 3-steps approach. See text for more explanations.



Set velocity by simulation [m/s]

Figure 4: Estimated wind velocity using Eq. 20 as function of YAO values. Each group of samples located at a single simulation velocity corresponds to a different phase screen with a different wind direction.

noise. We expect to include the convergence effect of measurements into our calibration. Using a proportional regression of the ratio d/τ versus v , we get the following calibration:

$$\hat{v} \simeq 0.882 \times \frac{d}{\tau}. \quad (20)$$

We report in Fig. 4 the wind-speed estimated using Eq. 20 versus the set value in YAO. We consider this calibration as acceptable for our next PSF-R purpose.

3.3.2 MMSE layer-by-layer reconstruction

To get the wind-speed profile, we perform a MMSE reconstruction of WFS slopes at a given layer. We need thus two covariance matrices to derive the reconstructor $\mathbf{R}(h_l)$ to get the phase at an altitude h :

$$\mathbf{R}(h_l) = \Sigma_{ss}(h_l) \times \left(\sum_{l=1}^{n_l} \Sigma_{ss}(h_l) \right)^{-1}, \quad (21)$$

where $\Sigma_{ss}(h_l)$ is the covariance matrix of all slopes, coming from both NGS/LGS WFS, for a sole turbulent layer at the altitude h_l . It is computed analytically using the model presented in Sect. 2.1. We then estimate the l^{th} turbulent layer contribution to the WFS measurements.

$$\hat{\mathbf{S}}(h_l) = \mathbf{R}(h_l) \times \mathbf{S} \quad (22)$$

Using the wind-speed estimation routine in Sect. 3.3.1 on $\hat{\mathbf{S}}(h_l)$, we estimate the wind-speed at altitude h_l .

4. WHT SITE CHARACTERIZATION

With the L3S method (see Sect. 2) and our wind-speed profile retrieval (see. Sect. 3.3), we have processed about 2,000 data sets acquired by CANARY in May 23, 24 and 25, in July 17,18,19, 22, 23 and 24 and in September 13, 15, 16, 17 and 18 of September 2013. See Sect. 3.2 and (10) for more information about the CANARY design.

On each data set, we have retrieved the seeing, outer scale and wind-speed profiles over five layers. The left panels of Fig. 5 show the distribution of the turbulence along the altitude as a kind of a probability density. Each point is a retrieved layer.

Using the auto-correlation of slopes, it is possible to get an estimation of the seeing above 20 km, the maximal altitude we can reconstruct by tomography with CANARY. We have gathered the seeing of such very high altitude layers into the 20 km plateau in Fig. 5.

In addition, we report on the right panels of Fig. 5 histograms of seeing, outer scale and wind-speed. We have split the turbulence into a ground part, altitude below 1 km, and an altitude part. For each retrieved turbulent profile, we have then averaged the ground and altitude values to analyze the turbulence behavior, differently if it comes from the ground or the altitude. To do that, we define the *effective outer scale* as :

$$L_0^* = \left(\frac{\sum_l L_0^{-5/3}(h_l) \times r_0^{-5/3}(h_l)}{\sum_l r_0^{-5/3}(h_l)} \right)^{-3/5}, \quad (23)$$

and the *coherent wind-speed*, coming from the coherent time of the turbulence, as:

$$v_0^* = \left(\frac{\sum_l v^{-5/3}(h_l) \times r_0^{-5/3}(h_l)}{\sum_l r_0^{-5/3}(h_l)} \right)^{-3/5}, \quad (24)$$

where the summation is done over all layers or altitude layers (above 1 km) or ground layers only. Eq. 23 and Eq. 24 gives integrated values of outer scale and wind speed in averaging the profile along layers in a same way than the r_0 computation (18).

The $r_0^{-5/3}$ is retrieved for any layers using the L3S approach. We report in Tab. 2 average values for seeing, layers contribution, effective outer scale and coherent wind-speed.

	Median values	1- σ std values
Global seeing	0.699 "	0.35 "
Ground seeing (h \leq 1.5 km)	0.552 "	0.32 "
Altitude seeing (1.5 km $>$ h \leq 20 km)	0.263 "	0.23 "
High Altitude seeing (h $>$ 20 km, appears in 16% of processed cases)	0.187 "	0.13 "
Ground contribution	76.8%	17%
Altitude contribution	22.2%	16.4%
High altitude contribution	7.46%	14.9%
Global L_0^*	8.9 m	8.4 m
Ground L_0^*	9.2 m	7.9 m
Altitude L_0^*	10.3 m	9.7 m
High Altitude L_0^*	12.9 m	13.1 m
Global v_0^*	3.07 m.s $^{-1}$	1.9 m.s $^{-1}$
Ground v_0^*	2.89 m.s $^{-1}$	1.9 m.s $^{-1}$
Altitude v_0^*	5.22 m.s $^{-1}$	2.78 m.s $^{-1}$

Table 2: Statistics on seeing at 500 nm, effective outer scale (see Eq. 23) and coherent wind-speed (see Eq. 24). It gives total values averaged over 2,000 data sets with ground and altitude layers contribution. Altitude and seeing are unbiased from the telescope airmass. Statistics on outer scale are given in throwing all outer values larger than 100 m, the software breakdown above which the outer scale retrieving is stuck.

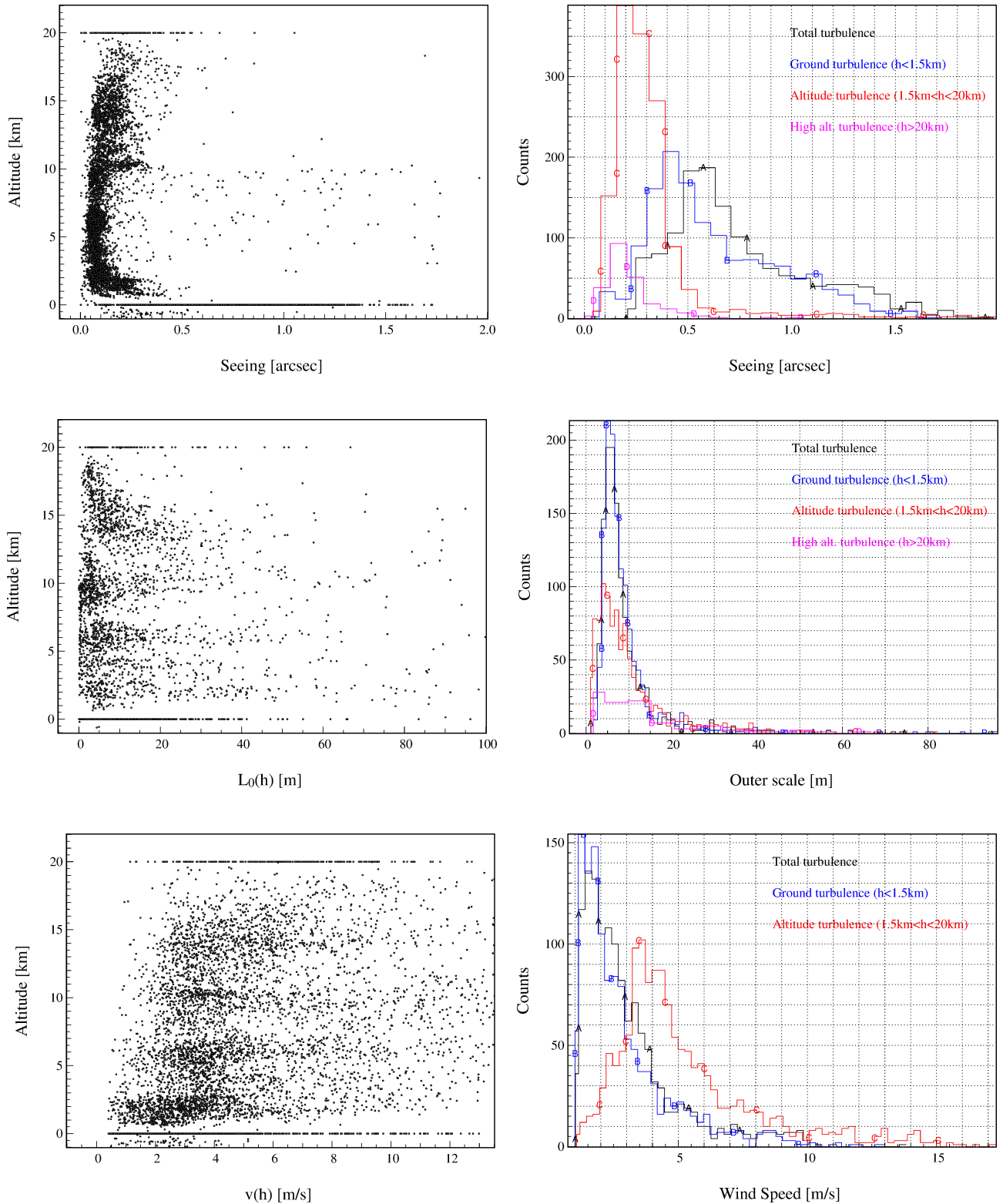


Figure 5: **Left:** Distribution of seeing, outer scale and wind-speed in altitude. Each point is a retrieved layer from one of the 5-layers profiles determined on 2,000 CANARY data sets. **Right:** Histogram of total, ground (below 1 km) and altitude turbulence characteristics. Each value has been averaged (see Eq. 23 and 24) over either ground turbulence (below 1 km) or altitude turbulence on a single data sets. The procedure has been repeated for all the 2,000 processed data sets. Values of seeing are unbiased from the airmass, as well as the altitude, and given at 500 nm of wavelength. All altitude layers retrieved above 20 km have been gathered into the plateau at 20 km.

As expected, the ground layer is the most dominant one with a median value of 76.8% of the total turbulence, while altitude layers, below 20 km represent about 22% of the turbulence. We get on average a ground seeing of 0.67", which is close to the reported value at the WHT (<http://www.ing.iac.es/Astronomy/telescopes/wht/>).

According to histograms in Fig. 5, the ground layer also dominates the seeing variability. Altitude layers below 20 km reach an average seeing of 0.26" and stay relatively constant in strength with time. We also notice negative altitude layers. They may appear between the WHT primary and secondary mirror, but we cannot determine if they really exist or if this is a LMA artifact.

Note the very altitude layers, above 20 km and too high for being reconstructed by tomography with CANARY, reach 7.5% of the total turbulence in median value, with 0.187" of seeing. However this only occurs in 16% of cases. It means this phenomena is not so frequent, but significant in terms of seeing.

Fig. 5 displays the vertical outer scale distribution. The relevance of the outer scale for tomography and PSF reconstruction is one of the actual preoccupation (See. paper 9909-16 *Review on AO real-time turbulence estimation* in that conference). The plot is less dense than the ones from the seeing and wind-speed distribution since 55% of samples have reached more than 100 m of outer scale. This is a software breakdown in the L3S code: above 100 m of outer scale, we no longer consider these is any physical meaning.

From the outer scale distribution, we draw two other observations: firstly, in more than 55% the L3S (and generally the L&A approach) retrieves an outer scale larger than 100 m. This is a software breakdown we have implemented into the spatial covariance model : if the LMA reaches this limit, we stick the value to 100 m, we consider there is no more physical meaning on that. In excluding those 55% of cases, we have 6% of cases that reach more than 20 m, 2.7% with more than 30 m and only 1% of cases with an outer scale greater than 50 m. The question now is why in 55% of cases is the L&A approach retrieved a fake value of the outer scale ?

A main reason is we are observing with a 4.2 m telescope and we are not sensitive to large values of outer scale. But now, we can wonder whether we are reaching the software breakdown of 100 m because the aperture-size of the telescope or because any other reason to be determined using end-to-end simulation.

Secondly, this distribution of $L_0(h)$ is quite constant around twice the telescope diameter and is constrained by the ground layer. Tab. 2 shows L_0^* becomes larger in altitude compared to the ground value. The conclusion on that is the estimation of the outer scale we have is biased by the finite aperture size from which we observe the turbulence.

In altitude, because the stars angular separations, the meta-pupil size is increasing with the altitude. It is exactly like the aperture-size through which we observe the turbulence is increasing as well, as the outer scale in altitude looks to do according to Fig. 5.

From those two observations, we conclude the estimation of the outer scale we are doing on a 4.2 m telescope is not directly related to a physical quantity. The problem we have now is to determine whether taking into account the entire outer scale profile is relevant for tomography and PSF-reconstruction on CANARY and demonstrate and understand why, using end-to-end simulations, the outer scale, as we have defined in Eq. 23, is twice the meta-pupil size.

Figure 5 illustrates the wind-speed profile as well. It appears the ground turbulence is the slowest one, with 2.89 m.s^{-1} , against 5.22 m.s^{-1} in altitude. We get a very strong variability of wind-speed values, especially in altitude, it makes thus the L3S approach more valuable.

Finally, the distributions of seeing, outer scale and wind-speed in Fig. 5 are denser around particular altitudes. These are the most contributing layers to the turbulence and are located at the ground, around 2 km, 6 km, 10 km and 16 km. The tomographic resolution we have on CANARY allows to retrieve on average five turbulent layers.

5. CONCLUSIONS

We have discussed on the L3S approach, an upgrade of the Learn& Apply algorithm, which dissociates the identification of the altitude layers from the ground layer. Under nominal observation conditions, the parameters it estimates lead to the same level of tomographic error than the L&A approach in using five time less temporal frames than the latter. Moreover, we can gain up to 30% on the tomographic error using the L3S.

The L3S technique has been applied over a large set of CANARY data to characterize the turbulence above the William Herschel Telescope (WHT): we find $0.67''/8.9\text{m}/3.07\text{m.s}^{-1}$ of total seeing/outer scale/wind-speed against $0.55''/9.2\text{m}/2.89\text{m.s}^{-1}$ below 1.5 km and $0.263''/10.3\text{m}/5.22\text{m.s}^{-1}$ between 1.5 and 20 km. We have also determined that the high altitude layers above 20 km, that cannot be compensated by CANARY, appear only 16% of time with a median seeing of $0.187''$. We have observed the outer scale values we can measure with CANARY are limited by around twice the meta-pupil size at a given altitude.

ACKNOWLEDGMENTS

The research leading to these results received the support of the A*MIDEX project (no. ANR-11-IDEX-0001-02) funded by the Investissements d’Avenir French Government program, managed by the French National Research Agency (ANR). This work is supported by CNRS, INSU, Observatoire de Paris, Université Paris Diderot-Paris 7 and the European Commission (Fp7 Infrastructures 2012-1, OPTICON Grant 312430, WP1).

REFERENCES

- [1] Ragazzoni, R., Marchetti, E. and Rigaut, F., *Modal tomography for adaptive optics*, Astron. & Astrophys. , 1999.
- [2] Neichel, B. and Fusco, T. and Conan, J.-M., *Tomographic reconstruction for wide-field adaptive optics systems: Fourier domain analysis and fundamental limitations*, Journal of the Optical Society of America A, 2008.
- [3] Vidal, F. , Gendron, E. and Rousset, G., *Tomography approach for multi-object adaptive optics*, JOSA A, 2010.
- [4] Wilson, R. W., *SLODAR: measuring optical turbulence altitude with a Shack-Hartmann wavefront sensor*, M.N.R.A.S , 2002.
- [5] Cortés, A. and Neichel, B. and Guesalaga, A. and Osborn, J. and Rigaut, F. and Guzman, D., *Atmospheric turbulence profiling using multiple laser star wavefront sensors*, M.N.R.A.S , 2012.
- [6] Lombardi, G. and Sarazin, M., *Using MASS for AO simulations: a note on the comparison between MASS and Generalized SCIDAR techniques*, M.N.R.A.S , 2016.
- [7] Shepherd, H. W., Osborn, J., Wilson, R. W., Butterley, T., Avila, R., Dhillon, V. S. and Morris, T. J., *Stereo-SCIDAR: optical turbulence profiling with high sensitivity using a modified SCIDAR instrument*, M.N.R.A.S , 2014.
- [8] Gendron, E. , Vidal, F. , Brangier, M. and Morris, T. , Hubert, Z. , Basden, A. , Rousset, G. , Myers, R. , Chemla, F. , Longmore, A. , Butterley, T. , Dipper, N. , Dunlop, C. , Geng, D. , Gratadour, D. , Henry, D. , Laporte, P. , Looker, N. , Perret, D. , Sevin, A. , Talbot, G. and Younger, E., *MOAO first on-sky demonstration with CANARY*, Astron. & Astrophys. , 2011,
- [9] Vidal, F. , Gendron, É. , Rousset, G. , Morris, T. , Basden, A. , Myers, R. , Brangier, M. , Chemla, F. , Dipper, N. , Gratadour, D. , Henry, D. , Hubert, Z. , Longmore, A. , Martin, O. , Talbot, G. and Younger, E., *Analysis of on-sky MOAO performance of CANARY using natural guide stars*, Astron. & Astrophys. , 2014.
- [10] Morris, T. , Gendron, E. , Basden, A. , Martin, O. , Osborn, J. , Henry, D. , Hubert, Z. , Sivo, G. , Gratadour, D. , Chemla, F. , Sevin, A. , Cohen, M. , Younger, E. , Vidal, F. , Wilson, R. , Butterley, T. , Bitenc, U. , Reeves, A. , Bharmal, N. , Raynaud, H.-F. , Kulcsar, C. , Conan, J.-M. , Huet, J.-M. , Perret, D. , Dickson, C. , Atkinson, D. , Bailie, T. , Longmore, A. , Todd, S. , Talbot, G. , Morris, S. , Rousset, G. and Myers, R., *CANARY phase B: on-sky open-loop tomographic LGS AO results*, Proc. SPIE , 2014.
- [11] Martin, O. and Gendron, É. and Morris, T. and Basden, A. and Hubert, Z. and Gratadour, D. and Osborn, J. and Vidal, F. and Chemla, F. and Rousset, G. and Myers, R., *Detailed analysis of the Canary on-sky results at the WHT using Rayleigh laser guide stars*, Proc. SPIE , 2014.
- [12] Gendron, E. , Morel, C. , Osborn, J. , Martin, O. , Gratadour, D. , Vidal, F. , Le Louarn, M. and Rousset, G., *Robustness of tomographic reconstructors versus real atmospheric profiles in the ELT perspective*, Proc. SPIE , 2014.

- [13] Sivo, G. and Kulcsár, C. and Conan, J.-M. and Raynaud, H.-F. and Gendron, É. and Basden, A. and Gratadour, D. and Morris, T. and Petit, C. and Meimon, S. and Rousset, G. and Garrel, V. and Neichel, B. and van Dam, M. and Marin, E. and Carrasco, R. and Schirmer, M. and Rambold, W. and Moreno, C. and Montes, V. and Hardie, K. and Trujillo, C., *On-sky validation of an optimal LQG control with vibration mitigation: from the CANARY Multi-Object Adaptive Optics demonstrator to the Gemini Multi-Conjugated Adaptive Optics facility.*, American Astronomical Society Meeting Abstracts, 2015,
- [14] Osborn, J., *Scintillation correction for astronomical photometry on large and extremely large telescopes with tomographic atmospheric reconstruction*, M.N.R.A.S , 2015.
- [15] Butterley, T. and Wilson, R. W. and Sarazin, M., *Determination of the profile of atmospheric optical turbulence strength from SLODAR data*, M.N.R.A.S , 2006.
- [16] Ono, Y. H. and Akiyama, M. and Oya, S. and Lardiére, O. and Andersen, D. R. and Correia, C. and Jackson, K. and Bradley, C., *Multi time-step wavefront reconstruction for tomographic adaptive-optics systems*, JOSA A , 2016/
- [17] Martin, O. A. and Gendron., É. and Rousset, G., Gratadour, D. and Vidal, F. and Morris, T. J. and Basden, A. G. and Myers, R. M. and Correia, C. M. and Henry, D., *Wave-front error breakdown in LGS MOAO validated on-sky by CANARY*, Astron. & Astrophys. , 2016.
- [18] Roddier, F., *The effects of atmospheric turbulence in optical astronomy*, Progress in optics. Volume 19. Amsterdam, North-Holland Publishing Co., 1981, p. 281-376., 1981.